



Hetero-phase dendritic elemental phosphorus for visible light photocatalytic hydrogen generation

Chunxiao Wu^a, Ruixue Zhu^b, Wey Yang Teoh^c, Yuxi Liu^a, Jiguang Deng^a, Hongxing Dai^a, Lin Jing^{a,*}, Yun Hau Ng^{d,e,**}, Jimmy C. Yu^{f,*}

^a Beijing Key Laboratory for Green Catalysis and Separation, and Faculty of Environment and Life, Beijing University of Technology, Beijing 100124, China

^b School of Physical Science and Technology, ShanghaiTech University, Shanghai 201210, China

^c Particles and Catalysis Research Group, School of Chemical Engineering, The University of New South Wales, Sydney, NSW 2052, Australia

^d Shenzhen Research Institute, City University of Hong Kong, Shenzhen Hi-Tech Industrial Park, Nanshan District, Shenzhen 518057 China

^e School of Energy and Environment, City University of Hong Kong, Tat Chee Avenue, Kowloon, Hong Kong Special Administrative Region

^f Department of Chemistry, The Chinese University of Hong Kong, Shatin, New Territories, Hong Kong Special Administrative Region

ARTICLE INFO

Keywords:

Red phosphorus
Elemental photocatalyst
Hetero-phase
Photocatalytic hydrogen evolution

ABSTRACT

We demonstrate a carefully tailored elemental red phosphorus (red P) for a record-high photocatalytic hydrogen evolution rate of $1280 \mu\text{mol g}^{-1} \text{h}^{-1}$. This performance has even surpassed some of the established compound photocatalysts. Systematic studies reveal that the bismuth-catalyzed selective growth of the preferential crystal phases of red P leads to the formation of fibrous and Hittorf's phases at distinctive sites within the same photocatalyst particle of dendritic morphology: nanobranches of fibrous phase and main stems of Hittorf's phase. As each crystal phase possesses unique band energy potential, the intimate heterojunction between the two phases affords an effective built-in driving force for the efficient transportation of photoexcited charge carriers with suppressed charge trapping and recombination. The strategy in crystal phase engineering of red P as well as the understanding of its charge transportation properties in this work provides new insights into developing favorable elemental P-based materials for various photocatalytic applications.

1. Introduction

As a clean energy carrier, hydrogen plays an important role in decarbonizing societies. There is an increasing number of authorities worldwide to officially include hydrogen development roadmap in their strategies to achieve carbon neutrality [1–5]. Hydrogen production is, as expected, the critical initial process for the entire hydrogen-related technology and economy. It is environmentally meaningful only when the hydrogen is produced from non-fossil sources. For this reason, water appears to be a promising source of hydrogen. Water can be split into molecular hydrogen by various means while photocatalysis may offer the simplest way to achieve it [6–9].

Over the past decades, the research community has seen rapid development in the improved photocatalytic systems capable of producing hydrogen gas from various aqueous-based solutions under illumination. The development of visible light-triggered photocatalytic

materials has been a focal point of research as the benchmarking photocatalyst (i.e. TiO_2) is only ultraviolet active [10,11], hence its limited application. The search for visible light active photocatalyst has prompted the burgeoning growth of various classes of photoactive materials. Metal oxides, metal nitrides and metal sulfides are the most studied categories of photocatalyst [12–15], while some emerging new materials (including the existing materials with newly found photo-activity) have been discovered (e.g. carbocatalyst, polymeric photocatalyst, metal-organic frameworks and zeolite photocatalyst) [16–22]. Extending the classes of photoactive semiconductors to include pure elemental photocatalyst is an important pursuit in developing highly efficient solar-driven photocatalytic hydrogen evolution (PHE) systems. Nonetheless, photocatalyst made of single element (e.g. phosphorus, boron, and silicon) is rather unexplored despite possessing several competitive advantages [23–26].

Being an unconventional photocatalyst, elemental red P was found to

* Correspondence authors.

** Corresponding author at: Shenzhen Research Institute, City University of Hong Kong, Shenzhen Hi-Tech Industrial Park, Nanshan District, Shenzhen 518057 China.

E-mail addresses: jinglin@bjut.edu.cn (L. Jing), yunhau.ng@cityu.edu.hk (Y.H. Ng), jimyu@cuhk.edu.hk (J.C. Yu).

<https://doi.org/10.1016/j.apcatb.2022.121428>

Received 17 February 2022; Received in revised form 13 April 2022; Accepted 17 April 2022

Available online 20 April 2022

0926-3373/© 2022 Elsevier B.V. All rights reserved.

have reasonably narrow bandgap energy (1.5–2.4 eV) which enables its visible light absorption [27–29]. More interestingly, elemental red P shows a p-type semiconducting behavior coupled with an energetic conduction band position, which is ideal for the reduction of the proton (H^+) to hydrogen [30,31]. However, the abundant amorphous red P usually exhibits the lowest photoactivity toward PHE among the P allotropes assessed. Converting the bulky amorphous red P to small-sized crystalline red P with different crystal phases (e.g. Hittorf's P and fibrous red P) has been reported as an effective way to improve the activity of red P. Our group devoted pioneering efforts in examining the photoactivities according to the phosphorus allotropes (i.e. amorphous, fibrous and Hittorf's phases) which has led to the record highest PHE rate of $684 \mu\text{mol g}^{-1} \text{h}^{-1}$ among elemental photocatalysts in 2016 [32]. However, the reported PHE rate is at a lower par in comparison with the typical compound photocatalysts (e.g. $g\text{-C}_3\text{N}_4$, CdS and TiO_2) which PHE rate of over $1000 \mu\text{mol g}^{-1} \text{h}^{-1}$ can be obtained [33–41]. Pursuing or even exceeding the performance of the conventional photocatalytic system by red P has been the underlying motivation of this research.

Inspired by the formation mechanism of carbon nanotube on transition metal (e.g. Ni, Fe, Co) through chemical-vapor-deposition (CVD) [42–44], in this work, we discovered the natural growth of elemental P promoted by bismuth (Bi) as co-catalyst. Herein, we report for the first time the Bi-assisted CVD synthesis of highly active dendritic red P (DRP) photocatalysts with tailored morphological features and desired balance of crystal phases with intimate heterojunction. The resultant dendritic structure, which is composed of main stems spiked with lateral branches, has distinctive crystal phases. Hittorf's phase is formed in the main stems while the branches are made of the fibrous phase. Band position analyses confirm the more energetic conduction band (CB) in the fibrous phase while Hittorf's phase possesses deeper valence band (VB) energy. As both crystal phases are junctioned effectively at the stem-branch intersection, the alignment of band energy between the two crystal phases facilitates the effective built-in forces for charge separation, which affords an enhanced PHE activity. In particular, we recorded a visible light PHE rate of $1280 \mu\text{mol g}^{-1} \text{h}^{-1}$ for the DRP, which is the highest activity compared to the previous reports on elemental photocatalysts.

2. Experimental section

2.1. Samples preparation

The purification of commercial amorphous red P was proceeded according to the previous reports [32,45]. Typically, 200 mg pre-treated red P with different amounts of Bi (0, 50, 100, 200, and 400 mg) were mixed and compressed into “tablets” (Fig. S1a). Then, the “tablets” were placed in the vacuum-sealed quartz tubes and heated to 580°C (5°C min^{-1}) in the tube furnace. After keeping static at 580°C for 2 h, the tubes were stepwisely and slowly cooled to 300°C ($0.1^\circ\text{C min}^{-1}$) and then to 25°C (1°C min^{-1}), respectively. After that, the samples were washed with carbon disulfide/water solution several times to remove any by-products. Subsequently, the sample suspensions were ultrasonicated for 2 h and kept static for 1 h. The dark sediments (Bi) were removed and final products (red P) in the suspensions were collected after centrifugation and drying.

2.2. Characterization

The morphological structure of the as-prepared samples was investigated by using scanning electron microscopy (SEM, SEM450) equipped with the energy dispersive X-ray (EDX) spectrometer, transmission electron microscopy (TEM, CM200) and high-resolution TEM (HRTEM, CM200) outfitted with EDX spectrometer. X-ray diffraction (XRD) patterns of samples were recorded on XRD-MPD-Scherrer X-ray diffractometer using $\text{Cu K}\alpha$ irradiation in the 2θ range from 10° to 40° . Fourier transform infrared spectroscopy (FTIR, Spotlight 400 FT-IR) of samples

was taken in the transmittance mode in the spectral range $500\text{--}3500 \text{ cm}^{-1}$ with a resolution of 0.1 cm^{-1} . Ultraviolet-visible (UV-vis) spectra of the samples were performed using a Varian Cary100 scan spectrophotometer. X-ray photoelectron spectroscopy (XPS) was conducted on Krato Axis Ultra DLD with 150 W Al $\text{K}\alpha$ X-ray radiation. The Brunauer-Emmett-Teller (BET) measurements were performed on Micrometric Tristar 3000 system using nitrogen adsorption.

2.3. PHE experiments

50 mg sample was dispersed in 100 mL water solution containing 10 vol% methanol (hole sacrificial agent). 1 wt% Pt nanoparticles were photo-deposited on the surface of the samples. A 300 W Xenon lamp (PLS-SXE300D, Beijing Perfectlight Technology Co., Ltd.) was employed as the light source. The amount of H_2 generated from the PHE reaction was recorded by a gas chromatograph (Techcomp GC 7900). The apparent quantum yield (AQY) measurement was performed under monochromatic light irradiation of $\lambda = 420, 450, 500, 550$ and 600 nm and calculated by $\text{AQY} = (2 \times \text{number of evolved hydrogen molecules}) / (\text{number of incident photons}) \times 100\%$.

2.4. Photoelectrochemical measurements

2 mg samples were made into electrodes on the FTO glass substrates ($2 \times 2 \text{ cm}$ squares) by drop-casting. All photoelectrochemical experiments were performed in a typical three-electrode setup system with an Autolab potentiostat (Model PGSTAT302N) and a 300 W Xenon lamp (PLS-SXE300) as the light source. 0.1 M Na_2SO_4 was used as the electrolyte. The linear sweep voltammetry (LSV) was measured with a sweeping rate of 1 mVs^{-1} in the potential range of $-0.6\text{--}0.2 \text{ V}$ with light chopping. Electrochemical impedance spectroscopy (EIS) of the samples was performed in a frequency range from 10 MHz to 100 KHz under an open circuit potential and visible light irradiation.

2.5. Time-resolved femtosecond transient absorption (fs-TA) spectroscopy measurements

The fs-TA spectroscopy experiments were conducted on an automated data acquisition transient absorption spectrometer (Ultrafast, Helios) equipped with a commercial fs Ti/Sapphire regenerative amplifier laser system (Mai Tai, Spitfire-Pro, Spectra Physics Company). A 400 nm pump laser was employed as the photoexcitation light and the TA signals were monitored by a probing light with a wavelength range from 470 to 750 nm. The decay curves were analyzed under 550 nm by two-exponential function fitting.

3. Results and discussion

3.1. Synthesis and characterization

The detailed CVD synthetic procedure of the DRP is illustrated in Fig. 1a. Commercial red P (amorphous) was used as the starting precursor (P source), and the metallic Bi was employed as a structural directing agent for the formation of the red P dendrites. The mixture was compressed into a “tablet” (Fig. S1a) and sealed in a quartz tube under vacuum and heated to 580°C for 2 h. During the heating process, the solid red P was vaporized by sublimation, while the Bi powders melted at a high temperature. In the subsequent cooling period, condensed Bi particles acted as an effective platform to provide high-density sites for the growth of the red P (Fig. S2 and S3). By ultrasonication the sample suspension, the less dense red P dendrites were effectively detached from the heavy Bi segments (Fig. S4), and the former can be recovered from the top layer of the suspension (Fig. S1b) followed by centrifuging and drying.

By controlling the weight ratio of Bi metal to amorphous red P, the evolution of the dendritic structure can be observed in the SEM images

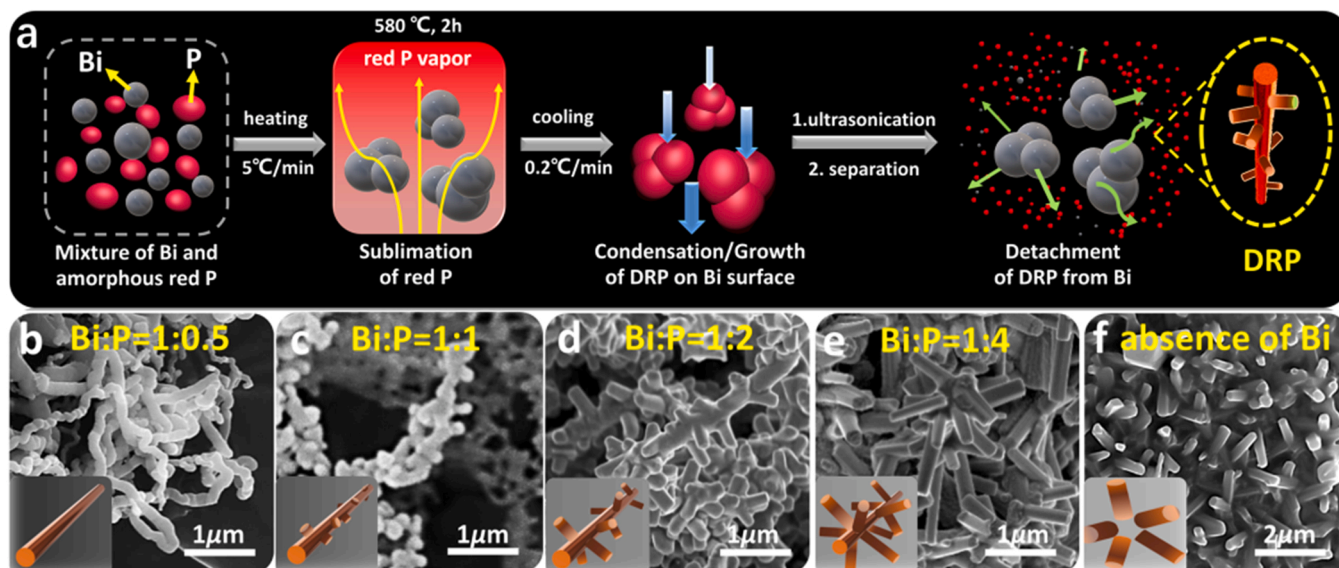


Fig. 1. (a) The CVD synthetic procedure of the DRP products. SEM images of the samples prepared with different precursor ratios of Bi to P: (b) red P nanowires (Bi: P = 1: 0.5), (c-e) DRP products (Bi: P = 1: 1, 1: 2 and 1: 4, respectively), and (f) red P nanorods (absence of Bi).

(Fig. 1b-e). In the P deficient environment (Bi: P = 1: 0.5), a uniform and tangled nanowire structure (ca. 90 nm in diameter) was obtained (Fig. 1b and S2). At a slightly higher red P content (Bi: P = 1: 1), nanorod-like branches started to grow on the nanowire-like stems to initiate the formation of the dendritic structure. With increasing the ratio of red P content (Bi: P = 1: 1 or 1: 2–1: 4), the apparent longer nanorod-like branches with higher density can be seen gradually

covering the main stems (Fig. 1c-e). In the absence of Bi, only red P nanorods were formed on the inner wall of the quartz tube (Fig. 1f). Moreover, all products after the CVD treatment showed significantly reduced particle sizes compared to the parental amorphous red P precursor ($> 5 \mu\text{m}$, Fig. S5), in which the smaller particles contributed to an improved surface area (Table S1).

Interestingly, the main stems and lateral branches of the DRP showed

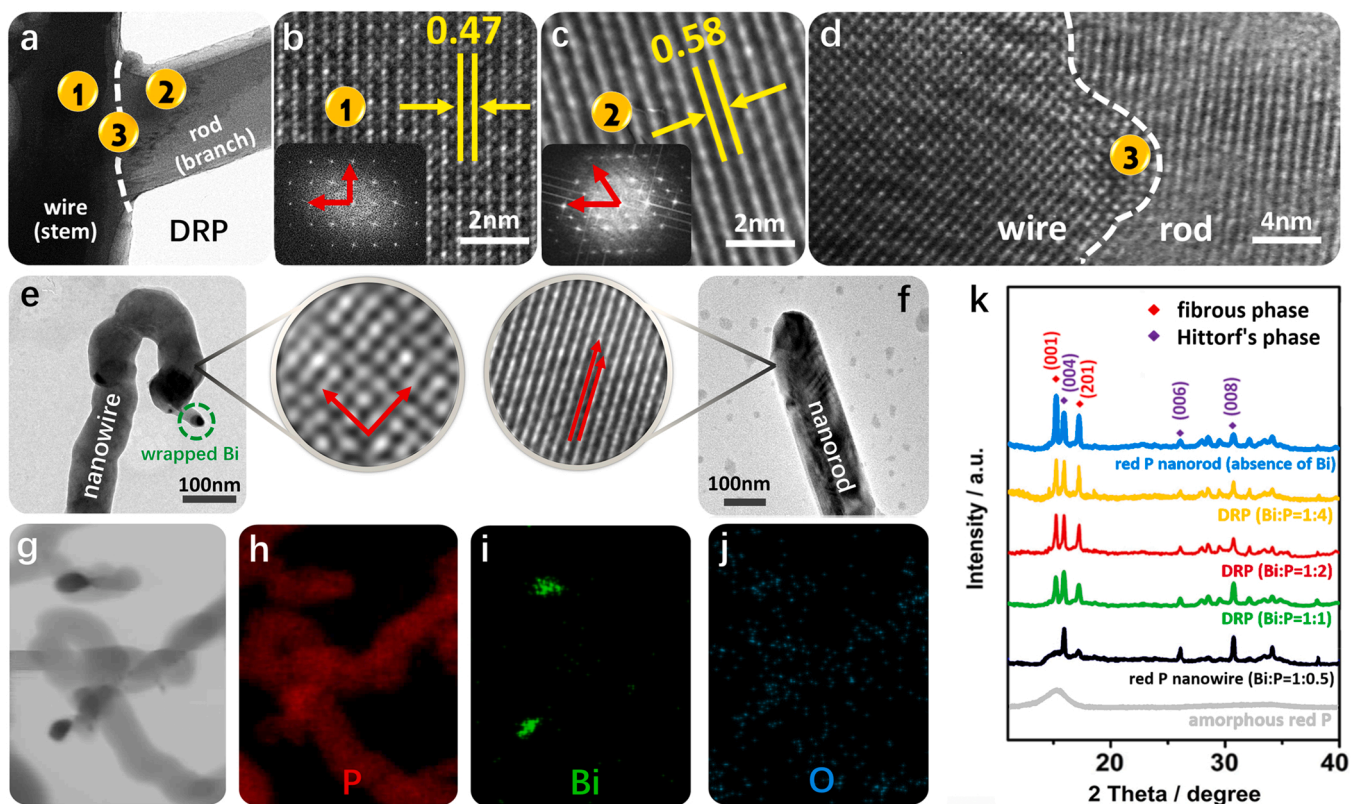


Fig. 2. (a) TEM image of the DRP sample (Bi: P = 1: 2), and (b-d) HRTEM images taken from the corresponding areas in (a); the corresponding FFT images are shown in the insets of (b) and (c). TEM and corresponding HRTEM images of (e) red P nanowire and (f) red P nanorod. (g) TEM and (h-j) corresponding EDX elemental mapping images of red P nanowire. (k) XRD spectra of the samples.

two different crystalline forms, as revealed by TEM (Fig. 2a) and HRTEM (Fig. 2b-d). The perpendicular strands from the stems correspond to the Hittorf's phase with a lattice space of 0.47 (004) (Fig. 2b), while the parallel arrangement of the branches with a lattice space of 0.58 (001) is typical of the fibrous phase (Fig. 2c). The corresponding fast Fourier transform (FFT) images (insets of Fig. 2b and c) further confirmed the orthogonal rows (angle amount $\sim 90^\circ$) of the Hittorf's phase and the skew rows (angle amount $\sim 55^\circ$) of the fibrous phase, respectively [46]. In addition, the transition of these two crystalline forms can be observed at the junctions between the stems and branches (Fig. 2d). The well-matched lattice fringes at the junction also indicated the epitaxial lateral growth of the fibrous phase on the Hittorf's phase. Bare Hittorf's phase was observed in the nanowire sample (Bi: P = 1: 0.5) while the nanorod sample (absence of Bi) was in the fibrous phase, respectively (Fig. 2e and f), indicating the formation of distinctive phases in different structures. The SEM and corresponding EDX analysis in Fig. S6 confirmed that the nanowires, dendrites and nanorods are mainly P, and no Bi signal could be detected on the surface of the samples. Moreover, the Bi 4f peaks can be hardly observed from the XPS survey analysis (Fig. S7a), which confirmed the successful removal of the large size Bi segment. Small Bi particles can be seen to be located and wrapped at the tips of the nanowires (Fig. 2e and g-j), suggesting the in-situ growth of red P nanowires from the Bi co-catalyst [47]. We noted that both the Hittorf's and fibrous phases have close layered structural relations, which are principally fabricated with the P chains containing P8 and P9 cages linking together to form tubular structures (Fig. S8) [28,48,49]. The P 2p XPS spectra of all of the red P nanowire (the Hittorf's phase), DRP (Bi: P = 1: 2) and red P nanorod (the fibrous phase) samples exhibited similar typical P 2p_{3/2} and P 2p_{1/2} peaks at binding energies of ca. 130.1 (± 0.02) and 130.9 (± 0.02) eV, respectively (Fig. S7b) [50, 51]. While the slight difference in intensity and location of these peaks can be attributed to the effects of the Van der Waals forces between the molecular structures in different phases [52,53]. In addition, all of the samples showed essentially similar FTIR spectra and no obvious vibration bands corresponding to the P-related functional groups (e.g., P-C, P-N, P-O, etc.) can be observed, indicating the similar P construction (Fig. S9).

XRD patterns of the products were compared in Fig. 2k. All the as-prepared samples showed sharp XRD peaks, indicating the crystallization of amorphous red P after the CVD treatment. In addition, the typical XRD peaks (Fig. S10) for the metallic Bi could hardly be observed on the as-prepared samples, further confirming the removal of the large-sized Bi after the ultrasonication treatment. We noted that both the Hittorf's and fibrous phases have similar XRD patterns [50,54]. For the red P nanowire sample (Bi: P = 1: 0.5), three main typical diffraction peaks from the (004), (006) and (008) planes can be observed, which match well with the characteristics of the Hittorf's phase [54,55]. Nevertheless, different crystalline facets are preferentially exposed on the fibrous phase. The peaks at 15.3° (001) and 17.2° (201) for the fibrous phase showed increased intensity with the increased number and length of the rod branches in the series of the DRP samples [29,30,32]. In addition,

crystallite sizes of the Hittorf's and fibrous phases were estimated to be 52 and 39 nm by using the Scherrer equation, respectively, indicating both nanowire and nanorod structures consisted of polycrystalline (detailed in Table S2). The XRD results were also consistent with the lattice spaces and fringes of these two phases, as shown in the HRTEM images (Fig. 2b-d).

3.2. Formation mechanism of the dendritic structure

Based on the above analysis, the formation process of the dendritic structure can be understood as illustrated in Fig. 3. According to the previous reports, the pure red P tends to form the fibrous phase structure in the CVD treatment [28,32,45]. In the presence of Bi, a small amount of the gasified red P gradually generated during the heating process was dissolved on the surface of the melted Bi, which subsequently induced the growth of the P with a nanowire structure in Hittorf's phase on the surface of condensed Bi beads during the cooling process. Although the exact growth mechanism of red P nanowires on the melted Bi is yet to be understood, it is believed to be analogous to the formation of carbon nanotubes in the presence of transition metal particles (e.g., nickel) which serve as the nucleation sites for further growth of elemental nanostructure (both carbon and phosphorus, respectively) [42,56]. While with the extension of P contents, the overloaded P was deposited and grown on the P nanowires (stems) to form the fibrous phase branches. The growth of the branches might be due to the lower surface energy of the (001) plane on the fibrous phase compared to that of (004) on the stems. Generally, the planes, which exhibit lower surface energies, would grow slower and have a higher tendency to survive during a prolonged growth process [57,58].

3.3. Energy band structure analysis

The optical properties of the red P nanowire (Hittorf's phase), DRP (Bi: P = 1: 2) and red P nanorod (fibrous phase) were performed by using the UV-vis spectroscopy (Fig. 4a). As expected, all of the samples possessed wide and strong absorption in the entire visible light region (400–800 nm). In addition, the samples with the increased amount of the fibrous phase showed slight redshifts in the absorption edge. The Kubelka-Munk plots (Fig. 4b) of the samples presented bandgaps of 1.84 and 1.71 eV of the red P nanowire and nanorod samples, respectively, which were consistent with the previous reports [28,59,60]. The slight difference in bandgap can be attributed to the different number of P layers in different phases [50]. In comparison, the DRP sample showed a bandgap of 1.76 eV, which can be attributed to the balanced construction between the Hittorf's phase "stems" and the fibrous phase "branches" in the dendritic structure. Valence XPS spectra of the red P nanowire and nanorod samples demonstrated the energy difference from VB to Fermi level is 1.08 eV and 0.69 eV, respectively (Fig. 4c and d). In addition, the LSV measurements (Fig. 4e and f) were performed to determine the on-set potential (Fermi level) of the red P nanowire and nanorod samples (-0.021 V and 0.024 V vs. Ag/AgCl at pH 7,

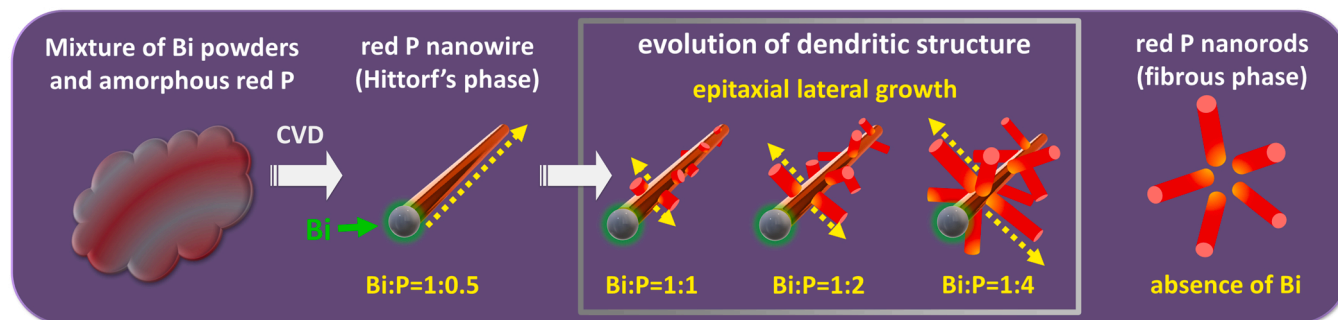


Fig. 3. Evolution of the structures and phases of the red P samples prepared with different precursor ratios of Bi to P.

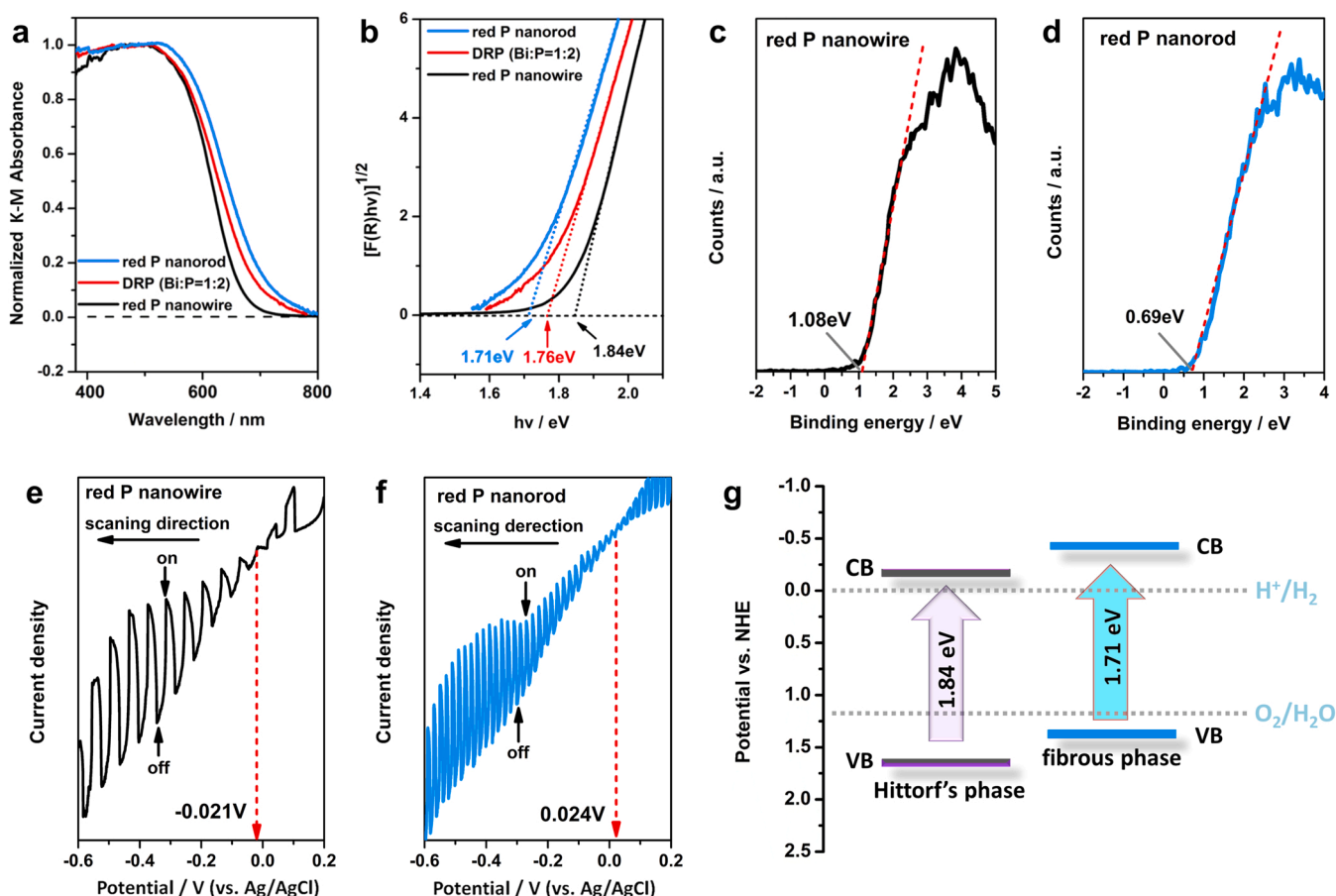


Fig. 4. (a) UV-vis spectra, (b) Kubelka-Munk plots, and (c, d) valence XPS spectra of the samples. (e, f) LSV measurement of the red P nanowire and red P nanorod samples with on-off illumination cycles. (g) The estimated bandgap structure of different phases.

respectively). The band energy structures (Fig. 4g) of the samples were further estimated by combining the above results (detailed experimental analyses to determine the band structure are shown in Table S3). Clearly, the band positions of both fibrous and Hittorf's phase red P are suitable for hydrogen production from water, and would be favourable for constructing an effective hetero-phase junction for efficient charge separation.

3.4. Photocatalytic activity

Encouraged by the above characterization results, PHE experiments were performed under visible light irradiation (> 420 nm, Fig. 5a). 1 wt % Pt was photo-deposited on the samples as the co-catalyst, and methanol was used as the sacrificial agent (holes scavenger). The effect of the residual Bi enwrapped within the samples on photocatalytic activity can be excluded, since Bi is photoinactive [61]. Under the above experimental conditions, the amorphous red P displayed an extremely low PHE yield of $79 \mu\text{mol g}^{-1} \text{h}^{-1}$. After crystallization, the series of the as-prepared samples exhibited an obviously increased PHE yield until the Bi: P ratio reached 1: 2. The DRP (Bi: P = 1: 2) sample showed the highest photocatalytic activity with PHE rate reaching $1280 \mu\text{mol g}^{-1} \text{h}^{-1}$, which was around 16 times higher than the amorphous red P and the best performance in various elemental photocatalysts and even competitive with many traditional compound photocatalysts (Fig. 5b, Table S4 and S5). The AQY of DRP (Bi: P = 1: 2) reached up to 3.51% at 420 nm (Fig. S11), which was higher than that of the bare red P nanowire/nanorod samples. Moreover, the DRP (Bi: P = 1: 2) sample showed stability of hydrogen production with ca. 10% decrease after 24 h recycling experiment (Fig. 5c). In addition, no noticeable changes in

morphological and chemical structure (Fig. S12 and S13) could be observed, indicating the dendritic structure and hetero-phase junction of DRP (Bi: P = 1: 2) are robust. With a higher ratio of P in the synthesis (Bi: P = 1: 4), however, a reduced PHE rate ($806 \mu\text{mol g}^{-1} \text{h}^{-1}$) was observed on the as-prepared DRP sample. According to the band alignment (Fig. 4g) of the hetero-phase heterojunction in DRP, the Hittorf's phase stems would act as the electron acceptor which provided the active sites for the PHE reaction. Therefore, the decreased photoactivity on the DRP (Bi: P = 1: 4) sample could be attributed to the greater coverage of the Hittorf's phase stems by the increased rod branches (as shown in Fig. 1e), which not only blocked the incident light to induce the charge excitation of the stems, but also restricted the exposure of the active sites on the stems. The solution-based EIS experiment was further conducted to probe the charge transfer resistance of the as-prepared samples (Fig. S14). Clearly, all the DRP samples exhibited smaller semicircles in the intermediate frequency than that of the bare red P nanowire / nanorod samples. This indicates the construction of effective hetero-phase junction and ordered structure in DRP contributed to the reduced interface resistance and hence promoted the charge carrier mobility.

3.5. Ultrafast spectra measurement and photocatalytic mechanism

The photo-charge dynamics of the samples were analyzed using the fs-TA spectroscopy by employing the pump-probe technique with a 400-nm laser as a pump pulse (50 fs) and a white light continuum of 470–750 nm as the probe pulse. According to the bandgap structure of the as-prepared samples as illustrated in Fig. 4g, all of the samples could be excited under 400 nm irradiation. Fig. 6a-c exhibited the fs-TA

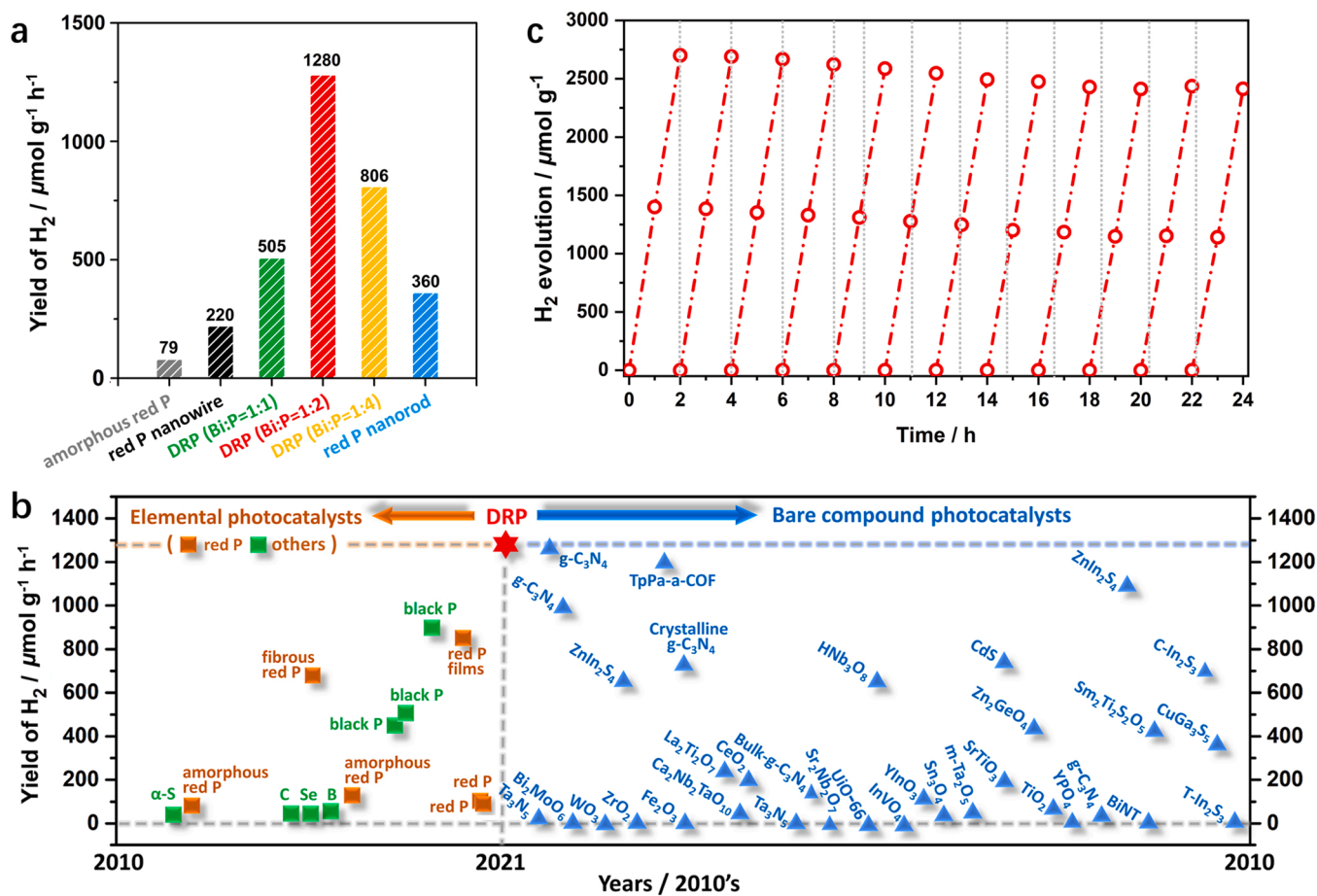


Fig. 5. (a) PHE yield of the as-prepared samples under visible light irradiation. (b) Comparison of visible light PHE rate between DRP and other bare elemental / compound photocatalysts. Detailed parameters are concluded in Table S4 and S5. (c) Photocatalytic stability of the DRP sample.

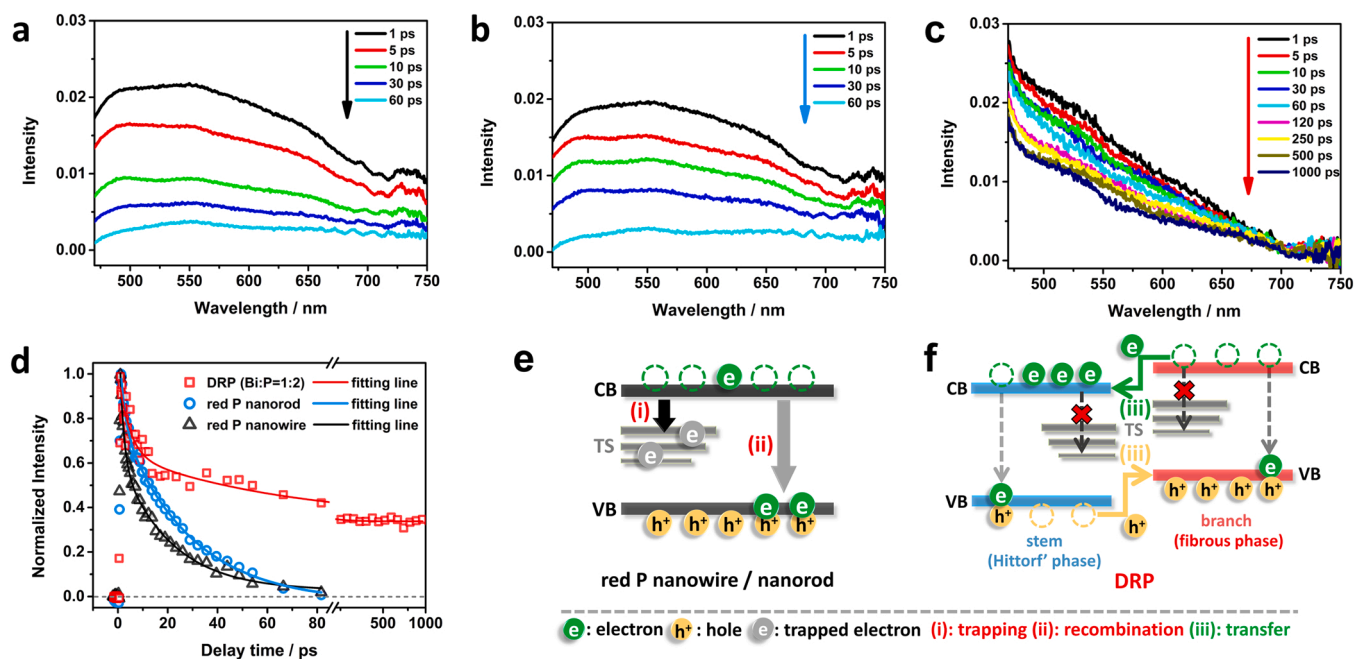


Fig. 6. Fs-TA spectra of (a) red P nanowire, (b) red P nanorod and (c) DRP (Bi: P = 1: 2) observed in visible light region under 400 nm light excitation. (d) Normalized fs-TA decay kinetics (dots) with exponential fitting curves (solid lines) of the sample dispersions (0.1 mg mL^{-1}) in H_2O probed at 550 nm under 400 nm excitation. Schematic representation of proposed charge dynamics in (e) red P nanowire / nanorod and (f) DRP.

spectra for the red P nanowire, red P nanorod and DRP (Bi: P = 1: 2), respectively. Upon the 400-nm photoexcitation, all of the samples showed broad and continuous absorption bands within the probe light range with a maximum at ca. 550 nm. For both the red P nanowire and red P nanorod samples, the absorption intensity rapidly decreased to nearly extinct within 80 ps (Fig. 6a and b). According to the previous study [29], these phenomena could be attributed to (i) the severe charge trapping process at deep trap states (TS) which are intrinsic to different crystal facets of red P, and (ii) the fast recombination of the charges in red P, both of which occur in ps time scale (Fig. 6e). In contrast, the DRP (Bi: P = 1: 2) sample exhibited a much slower decreased absorption signal within the first 80 ps, and the overall signal was maintained at over 38% in intensity for over 1000 ps (Fig. 6c).

For a better understanding of the charge dynamics of the samples during the photocatalytic process, kinetic traces of the photoinduced charges of each sample were recorded at 550 nm, as shown in Fig. 6d. The decay curves of the samples were well fitted by the two-exponential function with fitting parameters (e.g., lifetimes and portions) summarized in Table S6. At an early time scale, an ultrafast rise in the absorption signal was observed for all the samples within ca. 1 ps upon the pump laser excitation, which indicated instantaneous excitation and direct injection of the photo-charges from VB to CB of red P. In a period of 80 ps, both the red P nanowire and red P nanorod samples exhibited fast decay in TA intensity. The lifetimes of the charges for the red P nanowire were observed to be 1.6 ps (τ_1 , 54%) and 20.5 ps (τ_2 , 46%), while 2.0 ps (τ_1 , 33%) and 27.7 ps (τ_2 , 67%) for the red P nanorod (Table S6). The faster decay component (τ_1) of both samples can be attributed to the charge trapping into deep and photocatalytically inactive TS of red P [62]. The slower component (τ_2) can be assigned to the charge recombination. In comparison, the decay lifetimes in DRP (Bi: P = 1: 2) were much longer than that of the red P nanowire and red P nanorod [63]. The longer first component decay of $\tau_1 = 5.3$ ps (57%) in DRP (Bi: P = 1: 2) indicated a new decay process, which can be attributed to the transfer of photo-charges at the interface of the Hittorf-phase “stems” and fibrous-phase “branches”, which strongly restricted the charge self-trapping process of each portion (Fig. 6f). Moreover, the longer lifetime of $\tau_2 = 67$ ps (43%) and the plateau of 38% in the TA intensity (after 200 ps) indicated a prolonged charge recombination process in DRP (Bi: P = 1: 2). According to the growth mechanism of the dendritic structure (as illustrated in Fig. 3), the connection between the “stems” and “branches” is a tightly interior surface bonding rather than the normal exterior physical surface contact pattern. This greatly promoted the effective charge redistribution and transfer within DRP (Bi: P = 1: 2), which resulted in prolonged lifetimes of the photoactive charges for the enhanced PHE performance.

4. Conclusions

In summary, we for the first time report the synthesis of the dendritic elemental red P photocatalysts using a one-step CVD strategy with the assistance of Bi as a catalyst. The evolution of the crystal phases and morphologic features of red P from the Hittorf's phase nanowire to the final Hittorf's-fibrous hetero-phase dendritic structure can be rationally adjusted by Bi co-catalyst. The resulted DRP product was found to consist of the Hittorf's phase in the main stems and the fibrous phase in the lateral branches. The intimate interface between the “stems” and “branches” as well as the presence of band energy alignment contributed to the efficient charge transfer of the DRP, which significantly extended the lifetime of the active charges by restricting the charge recombination and self-trapping in each portion. As a result, superior and stable PHE performance was achieved in the DRP product. The strategy in crystal phase engineering of red P as well as the understanding of its charge transportation properties in this present work may provide new insights into developing other elemental photocatalysts for various photocatalytic applications.

CRediT authorship contribution statement

Chunxiao Wu: Investigation, Data curation, Formal analysis. **Ruixue Zhu:** Data curation. **Wey Yang Teoh:** Data curation. **Yuxi Liu:** Methodology. **Jiguang Deng:** Methodology. **Hongxing Dai:** Writing – review & editing. **Lin Jing:** Methodology, Investigation, Supervision, Project administration, Writing – review & editing. **Yun Hau Ng:** Writing – review & editing, Supervision. **Jimmy C. Yu:** Writing – review & editing, Supervision.

Declaration of Competing Interest

The authors declare that they have no known competing financial interests or personal relationships that could have appeared to influence the work reported in this paper.

Acknowledgements

This work was financially supported by the National Natural Science Foundation of China (Grant No. 51902008), Beijing Natural Science Foundation (Grant No. J210006), Research Funds for High-Level Talents (Grant No. 005000514119046), the General Program of Science and Technology Innovation Committee of Shenzhen Municipality (Grant No. JCYJ20190808181805621), Hong Kong Research Grants Council (RGC) General Research Fund (GRF) (Grant No. 11305419, 11306920 and 14307620).

Appendix A. Supporting information

Supplementary data associated with this article can be found in the online version at doi:10.1016/j.apcatb.2022.121428.

References

- [1] Y. Li, X. Bai, D. Yuan, F. Zhang, B. Li, X. San, B. Liang, S. Wang, J. Luo, G. Fu, General heterostructure strategy of photothermal materials for scalable solar-heating hydrogen production without the consumption of artificial energy, *Nat. Commun.* 13 (2022) 776, <https://doi.org/10.1038/s41467-022-28364-y>.
- [2] X. Li, W. Bi, L. Zhang, S. Tao, W. Chu, Q. Zhang, Y. Luo, C. Wu, Y. Xie, Single-atom Pt as co-catalyst for enhanced photocatalytic H₂ evolution, *Adv. Mater.* 28 (2016) 2427–2431, <https://doi.org/10.1002/adma.201505281>.
- [3] D.W. Wakerley, M.F. Kuehnle, K.L. Orchard, K.H. Ly, T.E. Rosser, E. Reisner, Solar-driven reforming of lignocellulose to H₂ with a CdS/CdO_x photocatalyst, *Nat. Energy* 2 (2017) 17021, <https://doi.org/10.1038/nenergy.2017.21>.
- [4] J. Liu, X. Zheng, L. Pan, X. Fu, S. Zhang, S. Meng, S. Chen, Efficient photocatalytic H₂ production coupling with selective oxidation of aromatic alcohol under carbon neutrality, *Appl. Catal. B* 298 (2021), 120619, <https://doi.org/10.1016/j.apcatb.2021.120619>.
- [5] D. Yuan, Y. Peng, L. Ma, J. Li, J. Zhao, J. Hao, S. Wang, B. Liang, J. Ye, Y. Li, Coke and sintering resistant nickel atomically doped with ceria nanosheets for highly efficient solar driven hydrogen production from bioethanol, *Green Chem.* 24 (2022) 2044–2050, <https://doi.org/10.1039/d1gc03955e>.
- [6] P. Ganguly, M. Harb, Z. Cao, L. Cavallo, A. Breen, S. Dervin, D.D. Dionysiou, S. C. Pillai, 2D nanomaterials for photocatalytic hydrogen production, *ACS Energy Lett.* 4 (2019) 1687–1709, <https://doi.org/10.1021/acsenenergylett.9b00940>.
- [7] S. Li, Y.H. Ng, R. Zhu, S. Lv, C. Wu, Y. Liu, L. Jing, J. Deng, H. Dai, In situ construction of elemental phosphorus nanorod-modified TiO₂ photocatalysts for efficient visible-light-driven H₂ generation, *Appl. Catal. B* 297 (2021), 120412, <https://doi.org/10.1016/j.apcatb.2021.120412>.
- [8] F.X. Xiao, J. Miao, H.B. Tao, S.F. Hung, H.Y. Wang, H.B. Yang, J. Chen, R. Chen, B. Liu, One-dimensional hybrid nanostructures for heterogeneous photocatalysis and photoelectrocatalysis, *Small* 11 (2015) 2115–2131, <https://doi.org/10.1002/sml.201402420>.
- [9] H. Suzuki, M. Higashi, H. Kunioku, R. Abe, A. Saeki, Photoconductivity–lifetime product correlates well with the photocatalytic activity of oxyhalides Bi₄TaO₈Cl and PbBiO₂Cl: an approach to boost their O₂ evolution rates, *ACS Energy Lett.* 4 (2019) 1572–1578, <https://doi.org/10.1021/acsenenergylett.9b00793>.
- [10] C. Peng, P. Wei, X. Li, Y. Liu, Y. Cao, H. Wang, H. Yu, F. Peng, L. Zhang, B. Zhang, K. Lv, High efficiency photocatalytic hydrogen production over ternary Cu/TiO₂@Ti₃C₂T_x enabled by low-work-function 2D titanium carbide, *Nano Energy* 53 (2018) 97–107, <https://doi.org/10.1016/j.nanoen.2018.08.040>.
- [11] X. Kong, Y. Xu, Z. Cui, Z. Li, Y. Liang, Z. Gao, S. Zhu, X. Yang, Defect enhances photocatalytic activity of ultrathin TiO₂ (B) nanosheets for hydrogen production by plasma engraving method, *Appl. Catal. B* 230 (2018) 11–17, <https://doi.org/10.1016/j.apcatb.2018.02.019>.

- [12] M. Kim, J. Lee, M. Je, B. Heo, H. Yoo, H. Choi, J. Choi, K. Lee, Electric field-driven one-step formation of vertical p–n junction TiO₂ nanotubes exhibiting strong photocatalytic hydrogen production, *J. Mater. Chem. A* 9 (2021) 2239–2247, <https://doi.org/10.1039/d0ta10062e>.
- [13] J. Cui, Y. Qi, B. Dong, L. Mu, Q. Ding, G. Liu, M. Jia, F. Zhang, C. Li, One-pot synthesis of BaMg_{1/3}Ta_{2/3}O_{3-x}N_y/Ta₃N₅ heterostructures as H₂-evolving photocatalysts for construction of visible-light-driven Z-scheme overall water splitting, *Appl. Catal. B* 241 (2019) 1–7, <https://doi.org/10.1016/j.apcatb.2018.09.014>.
- [14] L. Yin, X. Hai, K. Chang, F. Ichihara, J. Ye, Synergetic exfoliation and lateral size engineering of MoS₂ for enhanced photocatalytic hydrogen generation, *Small* 14 (2018), 1704153, <https://doi.org/10.1002/smll.201704153>.
- [15] Y. Li, J. Hao, H. Song, F. Zhang, X. Bai, X. Meng, H. Zhang, S. Wang, Y. Hu, J. Ye, Selective light absorber-assisted single nickel atom catalysts for ambient sunlight-driven CO₂ methanation, *Nat. Commun.* 10 (2019) 2359, <https://doi.org/10.1038/s41467-019-10304-y>.
- [16] M.A. Catherine, R.S. Sprick, A.I. Cooper, Emulsion polymerization derived organic photocatalysts for improved light-driven hydrogen evolution, *J. Mater. Chem. A* 7 (2019) 2490–2496, <https://doi.org/10.1039/C8TA11383A>.
- [17] J.-Z. Cheng, L.-L. Liu, G. Liao, Z.-Q. Shen, Z.-R. Tan, Y.-Q. Xing, X.-X. Li, K. Yang, L. Chen, S.-Y. Liu, Achieving an unprecedented hydrogen evolution rate by solvent-exfoliated CPP-based photocatalysts, *J. Mater. Chem. A* 8 (2020) 5890–5899, <https://doi.org/10.1039/c9ta13514f>.
- [18] A. Liu, L. Gedda, M. Axelsson, M. Pavliuk, K. Edwards, L. Hammarström, H. Tian, Panchromatic ternary polymer dots involving sub-picosecond energy and charge transfer for efficient and stable photocatalytic hydrogen evolution, *J. Am. Chem. Soc.* 143 (2021) 2875–2885, <https://doi.org/10.1021/jacs.0c12654>.
- [19] Y. Wang, X. Liu, J. Liu, B. Han, X. Hu, F. Yang, Z. Xu, Y. Li, S. Jia, Z. Li, Y. Zhao, Carbon quantum dot implanted graphite carbon nitride nanotubes: excellent charge separation and enhanced photocatalytic hydrogen evolution, *Angew. Chem. Int. Ed.* 57 (2018) 5765–5771, <https://doi.org/10.1002/anie.201802014>.
- [20] N. Meng, J. Ren, Y. Liu, Y. Huang, T. Petit, B. Zhang, Engineering oxygen-containing and amino groups into two-dimensional atomically-thin porous polymeric carbon nitrogen for enhanced photocatalytic hydrogen production, *Energy Environ. Sci.* 11 (2018) 566–571, <https://doi.org/10.1039/c7ee03592f>.
- [21] H. Yang, J. Wang, J. Ma, H. Yang, J. Zhang, K. Lv, L. Wen, T. Peng, A novel BODIPY-based MOF photocatalyst for efficient visible-light-driven hydrogen evolution, *J. Mater. Chem. A* 7 (2019) 10439–10445, <https://doi.org/10.1039/c9ta02357g>.
- [22] N. Dubey, S.S. Rayalu, N.K. Labhsetwar, S. Devotta, Visible light active zeolite-based photocatalysts for hydrogen evolution from water, *Int. J. Hydrog. Energy* 33 (2008) 5958–5966, <https://doi.org/10.1016/j.ijhydene.2008.05.095>.
- [23] G. Liu, L.-C. Yin, P. Niu, W. Jiao, H.-M. Cheng, Visible-light-responsive beta-rhombohedral boron photocatalysts, *Angew. Chem. Int. Ed.* 52 (2013) 6242–6245, <https://doi.org/10.1002/anie.201302238>.
- [24] Z. Kang, C.H. Tsang, N.B. Wong, Z. Zhang, S.T. Lee, Silicon quantum dots: a general photocatalyst for reduction, decomposition, and selective oxidation reactions, *J. Am. Chem. Soc.* 129 (2007) 12090–12091, <https://doi.org/10.1021/ja075184x>.
- [25] M. Zhu, Y. Osakada, S. Kim, M. Fujitsuka, T. Majima, Black phosphorus: a promising two dimensional visible and near-infrared-activated photocatalyst for hydrogen evolution, *Appl. Catal. B* 217 (2017) 285–292, <https://doi.org/10.1016/j.apcatb.2017.06.002>.
- [26] Z. Shen, S. Sun, W. Wang, J. Liu, Z. Liu, J.C. Yu, A black–red phosphorus heterostructure for efficient visible-light-driven photocatalysis, *J. Mater. Chem. A* 3 (2015) 3285–3288, <https://doi.org/10.1039/c4ta06871h>.
- [27] C. Wu, L. Jing, J. Deng, Y. Liu, S. Li, S. Lv, Y. Sun, Q. Zhang, H. Dai, Elemental red phosphorus-based photocatalysts for environmental remediation: a review, *Chemosphere* 274 (2021), 129793, <https://doi.org/10.1016/j.chemosphere.2021.129793>.
- [28] Z. Hu, Z. Shen, J.C. Yu, Phosphorus containing materials for photocatalytic hydrogen evolution, *Green Chem.* 19 (2017) 588–613, <https://doi.org/10.1039/c6gc02825j>.
- [29] L. Jing, R. Zhu, Y.H. Ng, Z. Hu, W.Y. Teoh, D.L. Phillips, J.C. Yu, Visible-light photocatalysis and charge carrier dynamics of elemental crystalline red phosphorus, *J. Chem. Phys.* 153 (2020), 024707, <https://doi.org/10.1063/5.0013142>.
- [30] L. Jing, R. Zhu, D.L. Phillips, J.C. Yu, Effective prevention of charge trapping in graphitic carbon nitride with nanosized red phosphorus modification for superior photo(electro)catalysis, *Adv. Funct. Mater.* 27 (2017), 1703484, <https://doi.org/10.1002/adfm.201703484>.
- [31] F. Wang, W.K.H. Ng, J.C. Yu, H. Zhu, C. Li, L. Zhang, Z. Liu, Q. Li, Red phosphorus: an elemental photocatalyst for hydrogen formation from water, *Appl. Catal., B* 111–112 (2012) 409–414, <https://doi.org/10.1016/j.apcatb.2011.10.028>.
- [32] Z. Hu, L. Yuan, Z. Liu, Z. Shen, J.C. Yu, An elemental phosphorus photocatalyst with a record high hydrogen evolution efficiency, *Angew. Chem., Int. Ed.* 55 (2016) 9580–9585, <https://doi.org/10.1002/anie.201603331>.
- [33] C.-Q. Xu, W.-D. Zhang, K. Deguchi, S. Ohki, T. Shimizu, R. Ma, T. Sasaki, Construction of a push–pull system in g-C₃N₄ for efficient photocatalytic hydrogen evolution under visible light, *J. Mater. Chem. A* 8 (2020) 13299–13310, <https://doi.org/10.1039/c9ta13513h>.
- [34] S.K. Apte, S.N. Garaje, G.P. Mane, A. Vinu, S.D. Naik, D.P. Amalnerkar, B.B. Kale, A facile template-free approach for the large-scale solid-phase synthesis of CdS nanostructures and their excellent photocatalytic performance, *Small* 7 (2011) 957–964, <https://doi.org/10.1002/smll.201002130>.
- [35] Y. Hong, J. Zhang, X. Wang, Y. Wang, Z. Lin, J. Yu, F. Huang, Influence of lattice integrity and phase composition on the photocatalytic hydrogen production efficiency of ZnS nanomaterials, *Nanoscale* 4 (2012) 2859–2862, <https://doi.org/10.1039/c2nr30150d>.
- [36] Y. Zhang, L. Wu, X. Zhao, Y. Zhao, H. Tan, X. Zhao, Y. Ma, Z. Zhao, S. Song, Y. Wang, Y. Li, Leaf-mosaic-inspired vine-like graphitic carbon nitride showing high light absorption and efficient photocatalytic hydrogen evolution, *Adv. Energy Mater.* 8 (2018), 1801139, <https://doi.org/10.1002/aenm.201801139>.
- [37] P. Zhang, D. Luan, X.W. Lou, Fabrication of CdS frame-in-cage particles for efficient photocatalytic hydrogen generation under visible-light irradiation, *Adv. Mater.* 32 (2020), 2004561, <https://doi.org/10.1002/adma.202004561>.
- [38] J. Yang, A. Acharjya, M.-Y. Ye, J. Rabeah, S. Li, Z. Kochovski, S. Youk, J. Roeser, J. Grüneberg, C. Penschke, M. Schwarze, T. Wang, Y. Lu, R. Krol, M. Oschatz, R. Schomäcker, P. Saalfrank, A. Thomas, Protonated imine-linked covalent organic frameworks for photocatalytic hydrogen evolution, *Angew. Chem. Int. Ed.* 60 (2021) 19797–19803, <https://doi.org/10.1002/anie.202104870>.
- [39] W. Hu, W. Zhou, K. Zhang, X. Zhang, L. Wang, B. Jiang, G. Tian, D. Zhao, H. Fu, Facile strategy for controllable synthesis of stable mesoporous black TiO₂ hollow spheres with efficient solar-driven photocatalytic hydrogen evolution, *J. Mater. Chem. A* 4 (2016) 7495–7502, <https://doi.org/10.1039/c6ta01928e>.
- [40] C. Du, Q. Zhang, Z. Lin, B. Yan, C. Xia, G. Yang, Half-unit-cell ZnIn₂S₄ monolayer with sulfur vacancies for photocatalytic hydrogen evolution, *Appl. Catal. B* 248 (2019) 193–201, <https://doi.org/10.1016/j.apcatb.2019.02.027>.
- [41] Y. Sheng, W. Li, Y. Zhu, L. Zhang, Ultrathin perylene imide nanosheet with fast charge transfer enhances photocatalytic performance, *Appl. Catal. B* 298 (2021), 120585, <https://doi.org/10.1016/j.apcatb.2021.120585>.
- [42] Z.F. Ren, Z.P. Huang, J.W. Xu, J.H. Wang, P. Bush, M.P. Siegal, P.N. Provencio, Synthesis of large arrays of well-aligned carbon nanotubes on glass, *Science* 282 (1998) 1105–1107, <https://doi.org/10.1126/science.282.5391.1105>.
- [43] A.K. Chatterjee, M. Sharon, R. Banerjee, M. Neumann-Spallart, CVD synthesis of carbon nanotubes using a finely dispersed cobalt catalyst and their use in double layer electrochemical capacitors, *Electrochim. Acta* 48 (2003) 3439–3446, [https://doi.org/10.1016/s0013-4686\(03\)00427-4](https://doi.org/10.1016/s0013-4686(03)00427-4).
- [44] S. Zanganeh, M. Torabi, A. Kajaafvala, N. Zanganeh, M.R. Bayati, R. Molaei, H. R. Zargar, S.K. Sadrezaad, CVD fabrication of carbon nanotubes on electrodeposited flower-like Fe nanostructures, *J. Alloy. Compd.* 507 (2010) 494–497, <https://doi.org/10.1016/j.jallcom.2010.07.216>.
- [45] Z. Shen, Z. Hu, W. Wang, S.-F. Lee, D.K.L. Chan, Y. Li, T. Gu, J.C. Yu, Crystalline phosphorus fibers: controllable synthesis and visible-light-driven photocatalytic activity, *Nanoscale* 6 (2014) 14163–14167, <https://doi.org/10.1039/c4nr04250f>.
- [46] M. Ruck, D. Hoppe, B. Wahl, P. Simon, Y. Wang, G. Seifert, Fibrous red phosphorus, *Angew. Chem. Int. Ed.* 44 (2005) 7616–7619, <https://doi.org/10.1002/anie.200503017>.
- [47] R.A.L. Winchester, M. Whitty, M.S.P. Shaffer, Synthesis of pure phosphorus nanostructures, *Angew. Chem. Int. Ed.* 48 (2009) 3616–3621, <https://doi.org/10.1002/anie.200805222>.
- [48] H. Thurn, H. Krebs, Über struktur und eigenschaften der halbmateriale. XXII. die kristallstruktur des hittorfschen phosphors, *Acta Crystallogr. Sect. B Struct. Sci.* 25 (1969) 125–135, <https://doi.org/10.1107/s0567740869001853>.
- [49] F. Bachhuber, J. vonAppen, R. Dronskowski, P. Schmidt, T. Nilges, A. Pfizner, R. Wehrhich, The extended stability range of phosphorus allotropes, *Angew. Chem. Int. Ed.* 53 (2014) 11629–11633, <https://doi.org/10.1002/anie.201404147>.
- [50] Y. Zhu, J. Ren, X. Zhang, D. Yang, Elemental red phosphorus-based materials for photocatalytic water purification and hydrogen production, *Nanoscale* 12 (2020) 13297–13310, <https://doi.org/10.1039/d0nr01748e>.
- [51] S. Lv, Y.H. Ng, R. Zhu, S. Li, C. Wu, Y. Liu, Y. Zhang, L. Jing, J. Deng, H. Dai, Phosphorus vapor assisted preparation of P-doped ultrathin hollow g-C₃N₄ sphere for efficient solar-to-hydrogen conversion, *Appl. Catal. B* 297 (2021), 120438, <https://doi.org/10.1016/j.apcatb.2021.120438>.
- [52] F. Baumer, Y. Ma, C. Shen, A. Zhang, L. Chen, Y. Liu, D. Pfister, T. Nilges, C. Zhou, Synthesis, characterization, and device application of antimony-substituted violet phosphorus: a layered material, *ACS Nano* 11 (2017) 4105–4113, <https://doi.org/10.1021/acsnano.7b00798>.
- [53] A. Pfizner, Phosphorus remains exciting!, *Angew. Chem. Int. Ed.* 45 (2006) 699–700, <https://doi.org/10.1002/anie.200503603>.
- [54] Z. Chen, Y. Zhu, Q. Wang, W. Liu, Y. Cui, X. Tao, D. Zhang, Fibrous phosphorus: a promising candidate as anode for lithium-ion batteries, *Electrochim. Acta* 295 (2019) 230–236, <https://doi.org/10.1016/j.electacta.2018.10.062>.
- [55] Y. Zhu, C. Lv, Z. Yin, J. Ren, X. Yang, C.-L. Dong, H. Liu, R. Cai, Y.-C. Huang, W. Theis, S. Shen, D. Yang, A [001]-oriented hitorff's phosphorus nanorods/ polymeric carbon nitride heterostructure for boosting wide-spectrum-responsive photocatalytic hydrogen evolution from pure water, *Angew. Chem. Int. Ed.* 59 (2020) 868–873, <https://doi.org/10.1002/anie.201911503>.
- [56] S. Talapatra, S. Kar, S.K. Pal, R. Vajtai, L. Ci, P. Victor, M.M. Shaijumon, S. Kaur, O. Nalamasu, P.M. Ajayan, Direct growth of aligned carbon nanotubes on bulk metals, *Nat. Nanotechnol.* 1 (2006) 112–116, <https://doi.org/10.1038/nnano.2006.56>.
- [57] M.A. Khan, H.T. Jung, O.B. Yang, Synthesis and characterization of ultrahigh crystalline TiO₂ nanotubes, *J. Phys. Chem. B* 110 (2006) 6626–6630, <https://doi.org/10.1021/jp057119k>.
- [58] Y. Wang, J. Chen, P. Wang, L. Chen, Y.-B. Chen, L.-M. Wu, Syntheses, growth mechanism, and optical properties of [001] growing Bi₂S₃ nanorods, *J. Phys. Chem. C* 113 (2009) 16009–16014, <https://doi.org/10.1021/jp904448k>.
- [59] X. Bai, Y. Du, X. Hu, Y. He, C. He, E. Liu, J. Fan, Synergy removal of Cr (VI) and organic pollutants over RP-MoS₂/rGO photocatalyst, *Appl. Catal. B* 239 (2018) 204–213, <https://doi.org/10.1016/j.apcatb.2018.08.016>.
- [60] T. Muhmood, M. Xia, W. Lei, F. Wang, Under vacuum synthesis of type-I heterojunction between red phosphorus and graphene like carbon nitride with

- enhanced catalytic, electrochemical and charge separation ability for photodegradation of an acute toxicity category-III compound, *Appl. Catal. B* 238 (2018) 568–575, <https://doi.org/10.1016/j.apcatb.2018.07.029>.
- [61] Y. Liu, Z. Hu, J.C. Yu, Liquid bismuth initiated growth of phosphorus microbelts with efficient charge polarization for photocatalysis, *Appl. Catal. B* 247 (2019) 100–106, <https://doi.org/10.1016/j.apcatb.2019.01.092>.
- [62] S. Corby, R.R. Rao, L. Steier, J.R. Durrant, The kinetics of metal oxide photoanodes from charge generation to catalysis, *Nat. Rev. Mater.* 6 (2021) 1136–1155, <https://doi.org/10.1038/s41578-021-00343-7>.
- [63] I. Grigioni, K.G. Stamplecoskie, D.H. Jara, M.V. Dozzi, A. Oriana, G. Cerullo, P. V. Kamat, E. Selli, Wavelength-dependent ultrafast charge carrier separation in the $\text{WO}_3/\text{BiVO}_4$ coupled system, *ACS Energy Lett.* 2 (2017) 1362–1367, <https://doi.org/10.1021/acsenergylett.7b00216>.